

From structure to function: Mechanistic exploration of calcium and strontium in carbon-doped boron nitride for enhanced nitric oxide oxidation



Wanyu Zhang ^a, Huanhuan Bai ^a, Bibo Ma ^a, Lin Wang ^a, Yumei Zhang ^a, Qingzhi Luo ^a, Jing An ^a, Huiying Mu ^a, Huaiyu Zhang ^b, Yandong Duan ^{a,*}, Desong Wang ^{a,c, **}

^a Hebei Key Laboratory of Photoelectric Control on Surface and Interface, School of Sciences, Hebei University of Science and Technology, Shijiazhuang 050018, People's Republic of China

^b Institute of Computational Quantum Chemistry, College of Chemistry and Materials Science, Hebei Normal University, Shijiazhuang 050024, People's Republic of China

^c State Key Laboratory of Metastable Materials Science and Technology (MMST), Hebei Key Laboratory of Applied Chemistry, Yanshan University, Qinhuangdao 066004, People's Republic of China

ARTICLE INFO

Keywords:

Alkaline earth metal
Photocatalysis
Nitride oxide deep oxidation
Boron nitride
Reaction mechanism

ABSTRACT

Heterogeneous photocatalysis rarely employs main group metals as active centers due to the lack of available d orbitals. In this study, alkaline earth metal centers were introduced into a carbon-doped boron nitride framework, leading to an optimization of their electronic structure and successful activation of catalytic activity. Interestingly, these metal centers were found to effectively utilize d orbitals or d/p hybrid orbitals to activate O₂ and H₂O, thereby generating a wealth of reactive oxygen species (ROS), which efficiently convert NO to NO₃. In addition, the optimized alkaline earth metal structural unit can not only strengthen carrier separation, but also improve the adsorption behavior of NO₂ on the catalyst surface and promote its further conversion to NO₃. This research provides new insights into the design of highly active sites and the exploration of catalytic mechanisms for alkaline earth metals.

1. Introduction

Severe environmental issues, such as photochemical smog and acid rain, pose a significant threat to human well-being, health, and the long-term progress of society. Nitrogen oxides (NO_x) are a significant contributor to these issues [1–3]. Utilizing photocatalysis technology to transform nitrogen oxides (NO_x) into value-added products like HNO₃ is a viable approach for eliminating detrimental gases like NO at a ppb level and addressing environmental pollution [4,5]. Significant endeavors have been undertaken in recent years to investigate and advance the utilization of semiconductors for the purpose of photocatalytic removal of NO [6–11]. Unfortunately, the photocatalytic removal of NO remains unsatisfactory due to practical issues related to the discharge of toxic intermediates, the treatment of nitrification products, and the stability of catalysts.

The alkaline earth metals calcium (Ca), strontium (Sr), and barium

(Ba) typically possess a valence shell configuration of ns², making it challenging to regulate their electronic structures [12,13]. In 2018, Frenking and Zhou's group reported that the electrons of these metals have the ability to transition from the s orbital to the d orbital [14]. This transition leads to their behavior resembling that of transition metals, exhibiting unique structure and reactivity [15–20]. These properties of alkaline earth metals enable them to be crucial catalyst promoters, as they successfully regulate both catalytic activity and product distribution in many reactions. Alkaline earth metals have also been reported as semiconductor promoters in the field of photocatalysis. Dong and Sun's group revealed that the incorporation of Mg, Ca, Sr, and Ba creates a pathway for electric charge between the neighboring layers, resulting in an enhanced efficiency of charge transfer and improved photocatalytic activity for removing NO [21,22]. Additionally, the amino and imino groups on the surface are regarded as the primary sites for the adsorption of small molecules. Yu's group developed modifications in g-C₃N₄

* Corresponding author.

** Corresponding author at: Hebei Key Laboratory of Photoelectric Control on Surface and Interface, School of Sciences, Hebei University of Science and Technology, Shijiazhuang 050018, People's Republic of China.

E-mail addresses: yduan@iccas.ac.cn (Y. Duan), dswang06@126.com (D. Wang).

by introducing Sr doping at multiple sites [23]. Multi-site Sr doping enhances the transfer efficiency of photo-generated carriers and stimulates H_2O_2 to generate more $\cdot\text{OH}$, resulting in the efficient removal of NO. To the best of our knowledge, the monatomic catalysts based on alkaline earth metals in the s-region have not yet gained significant attention and exploration. Further investigation is required to enhance the catalytic activity and elucidate the reaction mechanism of the catalyst utilizing alkaline earth metal as the active center, as there is still ample scope for improvement.

Boron nitride two-dimensional nanomaterials have great potential in the fields of optoelectronics and catalysis due to their unique structure and properties [24–27]. Hexagonal boron nitride (h-BN) is called "white graphene", which is arranged by boron atoms and nitrogen atoms in the sp^2 hybrid honeycomb lattice. As an insulator with wide indirect band gap (5–6 eV), light absorption is limited to the deep ultraviolet range, which is not conducive to photocatalysis. Introducing carbon into BN (C-BN) is a simple and efficient method to endue BN photocatalytic properties [28–32]. Herein, we further introduced the alkaline earth metal Sr and Ca atoms into the C-BN catalyst matrix, thus obtaining the photocatalysts of Ca/C-BN and Sr/C-BN. This study conducted a comprehensive investigation into the impact of Sr and Ca chelating C-BN on enhancing the segregation of photogenerated charges and the stimulation of O_2 and H_2O , and also clarified the catalytic mechanism of alkaline earth metal sites in the process of NO oxidation. This information is highly significant for the advancement of more innovative and effective catalysts based on alkaline earth metals for the deep oxidation of NO.

2. Experimental Section

2.1. Materials

Deionized water was used in all experiments. Boric acid (H_3BO_3), glucose ($\text{C}_6\text{H}_{12}\text{O}_6$), melamine ($\text{C}_3\text{H}_6\text{N}_6$), anhydrous calcium chloride (CaCl_2) and strontium chloride hexahydrate ($\text{SrCl}_2 \cdot 6 \text{ H}_2\text{O}$) were obtained from Shanghai Aladdin Biochemical Technology Co., Ltd.

2.2. Preparation of Photocatalysts

C-BN was prepared by high temperature bubble pyrolysis method. Glucose (10.13 g), melamine (14.19 g), and boric acid (13.91 g) were dissolved in 600 mL water at 98 °C under stirring. After cooling to 90 °C, the mixture was kept at this temperature for 6 h and transferred to ice bath. The crystallized C-BN precursor was transferred to tubular furnace and calcined in N_2 atmosphere (900 °C, 2 h) to obtain gray powder (C-BN). Ca/C-BN and Sr/C-BN were synthesized following the same procedure except that 0.58 g anhydrous calcium chloride or 0.64 g strontium chloride hexahydrate was added in the process of mixing melamine, boric acid and glucose.

2.3. Characterization

The morphologies were characterized by scanning electron microscopy (SEM, TESCAN MIRA LMS), high resolution transmission electron microscopy (TEM, JEM 2100 F, JEOL), and aberration-corrected transmission electron microscopy (AC-TEM, JEM-ARM300F). X-ray photoelectron spectroscopy (XPS) measurements were carried out on Thermo Scientific K-Alpha. SmartLab-9 kW (Rigaku) was employed to perform X-ray diffraction (XRD) measurements. The scanning range for the measurements is from $2\theta = 5\text{--}100^\circ$. The Fourier-transform infrared spectroscopy (FTIR) of the samples were recorded on Prestige-21 FTIR spectrometer (Shimadzu) using KBr pellets. The actual content of Ca and Sr elements in Ca/C-BN and Sr/C-BN were analyzed by inductively coupled plasma optical emission spectroscopy (ICP-OES) system (720ES, Agilent). The reactive oxygen species (ROS) studies were conducted on electron spin-resonance spectroscopy (EMXplus-6/1, Bruker). Nitrogen

sorption measurement was performed using a Micromeritics ASAP 2460 system at 77 K. The K-edge information of Ca was obtained at the Singapore Synchrotron Radiation Facility (SSLS) and was measured in transmission mode. Sr K-edge analysis was performed with Si (111) crystal monochromators at the BL14W1 beamlines at the Shanghai Synchrotron Radiation Facility (SSRF) (Shanghai, China) and was recorded in transmission mode. The XAFS spectra of the standard sample (CaO and SrO) were recorded in transmission mode. The software codes Athena and Artemis were utilized to process and analyze the spectra. The INVENIO R FTIR spectrometer (Bruker) equipped with an in-situ diffuse reflectance cell (Harrick) was used to measure the in-situ FTIR spectra. Fluorescence spectra were recorded on F-4600 fluorescence spectrophotometer with excitation wavelength of 260 nm. Diffuse reflectance spectra (DRS) were obtained on UV-2550 spectrometer (Shimadzu). Electrochemical tests were performed on CHI660E electrochemical workstation (Shanghai Chenhua Instrument Co., Ltd, China). Electrochemical impedance spectroscopy (EIS) tests were carried out on a three-electrode system, using platinum wire as counter electrode, Ag/AgCl as reference electrode, and 0.2 M Na_2SO_4 as electrolyte.

2.4. Photocatalytic Oxidation of NO Activity Test

The evaluation of photocatalytic efficiency was conducted in a continuous-flow chamber utilizing simulated sunlight produced by a Xenon lamp. The initial concentration of NO was reduced to 500–600 ppb by regulating the air flow at a rate of 2.4 L min^{-1} and the NO flow at a rate of 15 mL min^{-1} . The glass plate was uniformly coated with the catalyst (200 mg) and subsequently inserted into the flow reactor. The simulated solar light source is vertically directed onto the photocatalyst through the quartz window of the reactor. A NO-NO₂-NO_x analyzer (42i-TL, THERMO FISHER, American) was used to continuously measure and determine the amount of NO_x at intervals of 1 min. The removal rate (η) of NO was determined using the formula: $\eta = 1 - (c/c_0) \times 100\%$, where c represents the current concentration of NO in ppb and c_0 is the concentration of NO after reaching adsorption-desorption equilibrium.

2.5. Computational Method

All density functional theory (DFT) calculations were performed based on the Vienna Ab-initio Simulation Package (VASP) [33,34] with a generalized gradient approximation (GGA) exchange-correlation functional (Perdew, Burke, and Ernzerhof, PBE)[35]. The plane wave cutoff energy was set to be 450 eV. A k-point mesh of $(3 \times 3 \times 3)$ was used and a vacuum layer of $> 15 \text{ \AA}$ was added to the z direction. DFT-D3 method with Becke-Jonson damping was used to describe van der Waals interactions [36,37]. The adsorption energy of was calculated as: $E_{\text{ads}} = E_{\text{adsorbate/catalyst}} - E_{\text{adsorbate}} - E_{\text{catalyst}}$, where $E_{\text{adsorbate/catalyst}}$ represents the total energy of the molecule adsorbed on the surface of C-BN, Ca/C-BN or Sr/C-BN, $E_{\text{adsorbate}}$ represents the energy of the adsorbed molecule, and E_{catalyst} represents the energy of C-BN, Ca/C-BN or Sr/C-BN. Gibbs free energies were calculated at 298.15 K from $G = E_{\text{DFT}} + E_{\text{ZPE}} - TS$, where E_{DFT} is the electronic energy calculated with VASP, E_{ZPE} is the zero-point energy and TS is the entropy contribution.

3. Results and discussion

3.1. Characterization of photocatalysts

A simple and scalable approach was used to synthesize the porous Ca, Sr embedded C-BN photocatalyst (Fig. 1a). Firstly, melamine as nitrogen source, boric acid as boron source, and glucose as carbon source were added to $\text{CaCl}_2 \cdot 6 \text{ H}_2\text{O}$ or $\text{SrCl}_2 \cdot 6 \text{ H}_2\text{O}$ aqueous solution and then dissolved, and crystallized to form the precursor of polymer network structure after cooling. The polymer network structure can provide abundant space to store and confine Ca/Sr elements, and then the

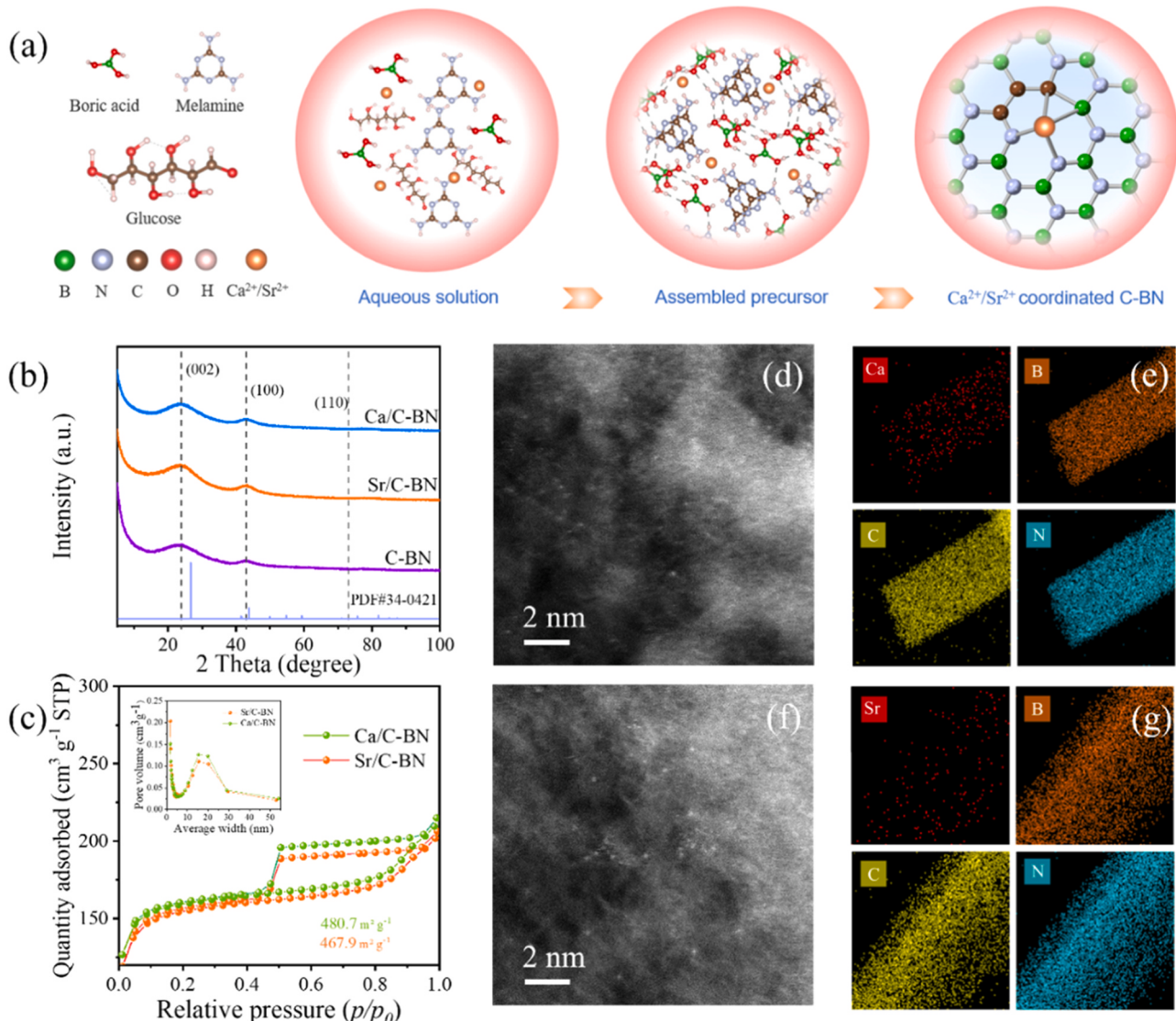


Fig. 1. (a) Synthesis diagram of Ca^{2+} , Sr^{2+} coordinated C-BN. (b) XRD data curves of C-BN, Ca/C-BN and Sr/C-BN. (c) N_2 adsorption-desorption isotherms and the corresponding pore size distribution plots of Ca/C-BN and Sr/C-BN. AC-TEM images of (d) Ca/C-BN and (f) Sr/C-BN. EDS elemental mapping images of (e) Ca/C-BN and (g) Sr/C-BN.

polymer network was pyrolyzed at a specific temperature to obtain the coordinated C-BN photocatalyst. Fig. 1b exhibits the XRD patterns of C-BN, Ca/C-BN, and Sr/C-BN. After introducing Ca or Sr into C-BN, no diffraction peak and other impurity peaks are found in the XRD patterns, which is attributed to the high dispersion of Ca or Sr species in the C-BN support. Moreover, the diffraction peaks at $20=26.6^\circ$, 43.7° , and 75.6° are consistent with those of C-BN, indicating that the material still retains the main structure of h-BN. ICP analysis reveals that the Ca/Sr content of Ca/C-BN and Sr/C-BN samples is 0.76 wt% and 0.84 wt%, respectively (Table S1). Typical SEM images of the samples in Fig. S1 show that the surface morphology of the samples is highly disordered and broken fibers, with a width of *ca.* 2–3 μm . TEM was further used to observe the morphology, as shown in Fig. S2–S3. Ca/C-BN and Sr/C-BN are fibrous structures with porous transparent dots on the surface, and the pore size is about 25 nm. The sample's pore structure and specific surface area were determined using a N_2 adsorption-desorption test, as depicted in Fig. 1c, S4. The adsorption isotherms have saturated adsorption platforms, which are H4 hysteresis loops with uniform surface pore size distribution. There is no significant difference in the pore size distribution between C-BN, Ca/C-BN, and Sr/C-BN, indicating that the addition of Ca or Sr atoms has limited influence on the structure of C-

BN. The formation of the pore structure is advantageous for enhancing the number of adsorption sites on the catalyst surface, thereby facilitating the NO oxidation reaction. Further AC-STEM measurement at sub-angstrom resolution was performed to elucidate the existence state of Ca and Sr atoms. As shown in Fig. 1d, f, due to the stronger scattering of Ca and Sr, a large number of highly dispersed points with stronger image contrast are observed, clearly showing the presence of Ca and Sr single atoms. The element mapping images demonstrate a homogeneous dispersion of elements B, N, C, O, and Ca/Sr in the catalyst (Fig. 1e, g, S5).

The X-ray absorption near-edge structure (XANES) spectrum provides insights into the oxidation state of Ca and Sr in the catalysts (Fig. 2a, d). The Ca and Sr K-edge absorption position of Ca/C-BN and Sr/C-BN catalyst is slightly lower compared to that of CaO and SrO, suggesting that the oxidation state of Ca/Sr is slightly below +2. As shown in Fig. 2b, e and Fig. S6–7, the Fourier-transformed extended X-ray absorption fine structure (FT-EXAFS) spectra of Ca/C-BN and Sr/C-BN catalyst exhibit one main peak at *ca.* 1.80 \AA and 1.89 \AA . No

obvious Ca-Ca and Sr-Sr coordination peaks are found at *ca.* 2.76 \AA and 3.30 \AA , confirming the existence of isolated single Ca/Sr atoms. The fitting structural parameters are summarized in Table S2. In order to

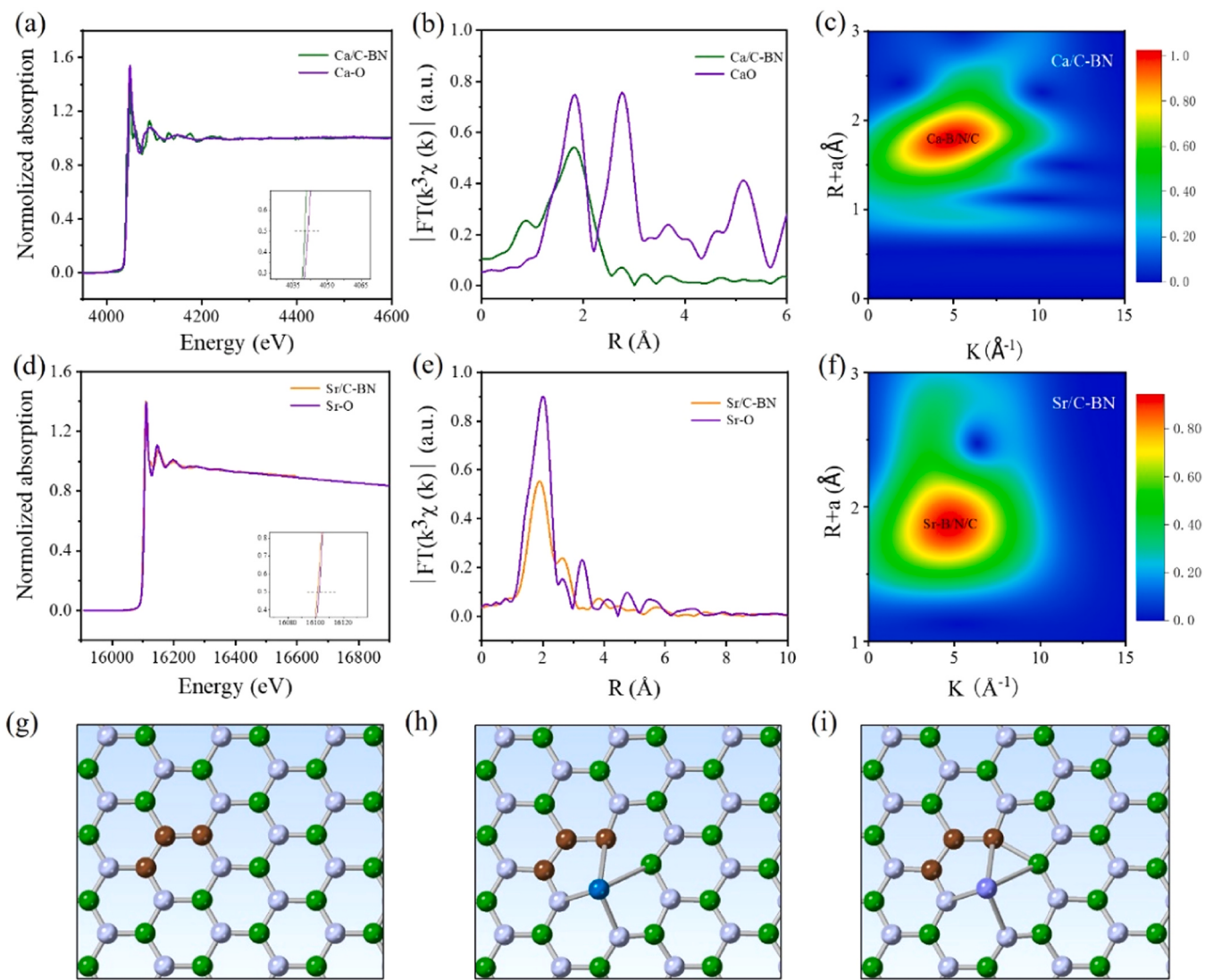


Fig. 2. The normalized Ca K-edge XANES spectra of (a) Ca/C-BN. Corresponding FT-EXAFS spectra of (b) Ca/C-BN. (c) WT contour plots of Ca K-edge at R space of Ca/C-BN. The normalized Sr K-edge XANES spectra of (d) Sr/C-BN. Corresponding FT-EXAFS spectra of (e) Sr/C-BN. (f) WT contour plots of Sr K-edge at R space of Sr/C-BN. (g) Image of C-BN atomic bonding structure. (h) Image of Ca/C-BN atomic bonding structure. (i) Image of Sr/C-BN atomic bonding structure.

strengthen these findings, we carried out wavelet transform (WT) analysis (Fig. 2c, f, S8). The WT diagram of Ca/C-BN and Sr/C-BN have only one maximum value of 5.0 Å⁻¹ and 4.7 Å⁻¹, which deviates notably from the WT diagrams seen for both CaO and SrO. This discrepancy provides more evidence supporting the notion of atomic dispersion of Ca/Sr species inside the Ca/C-BN and Sr/C-BN composite. The structural models of C-BN, Ca/C-BN and Sr/C-BN were constructed based on the XAFS results (Fig. 2g-i).

3.2. Charge transfer over photocatalysts

Fig. 3a-b displays the side and top views of the charge density difference for the Ca/C-BN and Sr/C-BN structures. The obvious charge redistribution in the Ca-C/B/N or Sr-C/B/N bond region indicates the obvious interaction between C-BN and Ca/Sr atoms. In addition, the distance between the Ca/Sr atom and the C-BN layer of Ca/C-BN and Sr/C-BN is 1.76 Å and 2.02 Å, respectively. The Ca/C-BN structure exhibits a broken mirror symmetry, resulting in the presence of an inherent dipole moment. This dipole moment causes an internal electric field that is oriented from the C-BN plane towards the protruding Ca/Sr atom. The electric field intensity can be quantitatively calculated by finite element method [38,39]. As shown in Fig. 3c, the electric field intensity near Ca

atom is higher than that near Sr atom, and an increased internal electric field is beneficial for the separation of photogenic charge carriers. The UV-vis DRS spectra, as shown in Fig. 3d, indicate a notable decrease in the absorption within the full region subsequent to the incorporation of Ca or Sr atom into the C-BN structure. The reduction of light absorption performance is not conducive to the progress of photocatalytic reaction. Therefore, the enhancement of photocatalytic performance in materials following the incorporation of Ca/Sr atoms may be attributed to other factors, such as improved efficiency of carrier separation and transport, as well as enhanced activation capabilities for O₂ and H₂O. Steady state photoluminescence (PL) spectra (Fig. 3e) evaluate the photogenerated electron dynamics under 260 nm excitation, in which Ca/C-BN and Sr/C-BN show obvious attenuated emission, which confirms the superior separation of photogenerated carriers. Meanwhile, the arc radius of Ca/C-BN and Sr/C-BN is relatively smaller than that of C-BN. This observation suggests that the carrier separation impedance is reduced and the photogenerated charge transfer occurs at a faster rate in Ca/C-BN and Sr/C-BN.

3.3. O₂ and H₂O activation

Based on the aforementioned experimental results, we performed

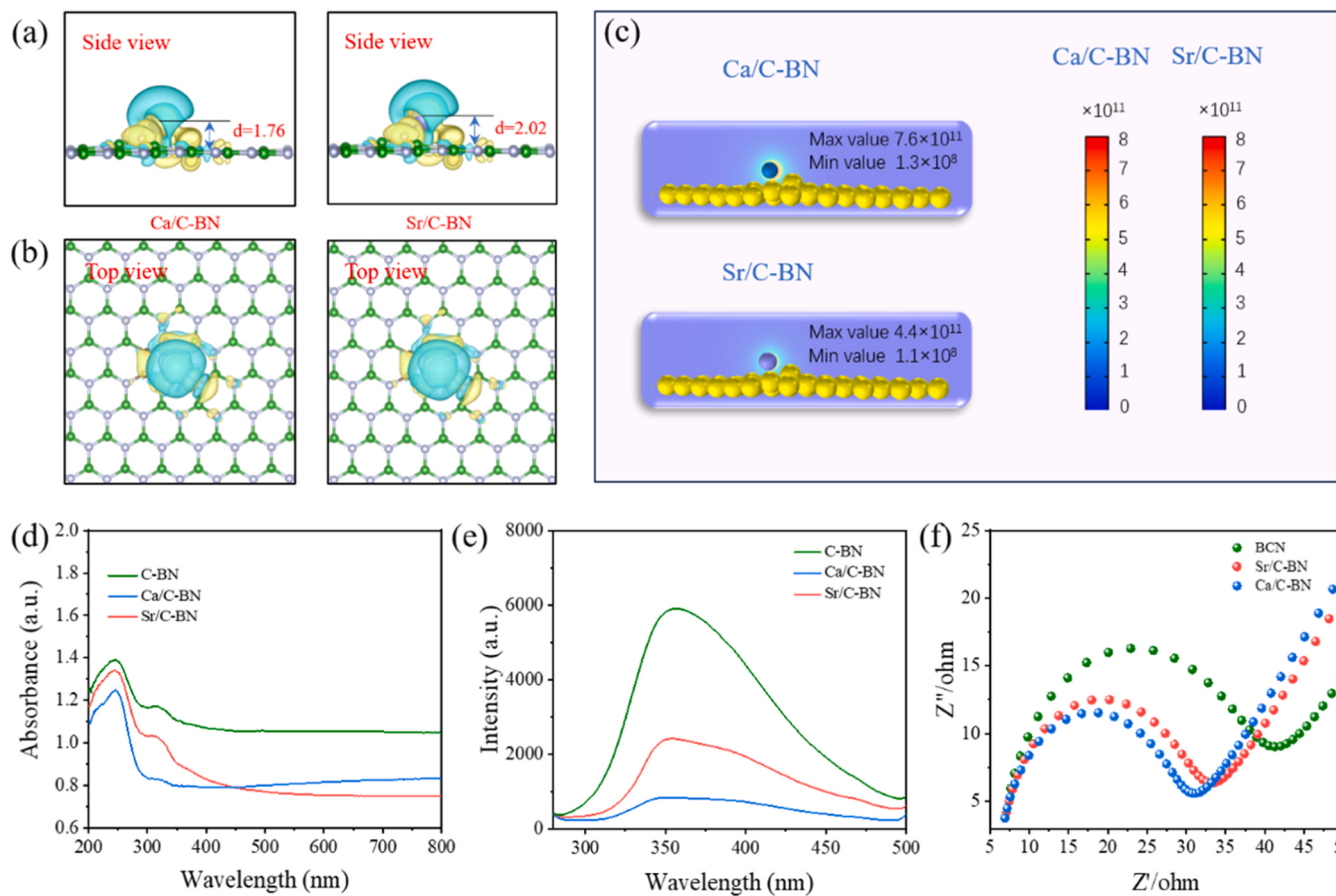


Fig. 3. (a)-(b) The differential charge density (yellow area refers to charge accumulation and blue area refers to charge loss) of Ca/C-BN and Sr/C-BN. (c) The electric field intensity calculated by finite element method. (d) UV-vis diffuse reflectance spectra of C-BN, Ca/C-BN and Sr/C-BN. (e) Photoluminescence spectra of C-BN, Ca/C-BN and Sr/C-BN. (f) EIS Nyquist plots of C-BN, Ca/C-BN and Sr/C-BN.

DFT calculations to examine the relationship between the structure and properties of C-BN, Ca/C-BN, and Sr/C-BN at the molecular surface level. Initially, we analyzed the adsorption energy and differential charge distribution of O_2 and H_2O molecules at the catalytic sites of C-BN, Ca/C-BN, and Sr/C-BN. (Fig. 4, S9-S11). Fig. 4a-c demonstrate that the adsorption capacity of O_2 is improved in Ca/C-BN and Sr/C-BN compared to C-BN. The adsorption energy of O_2 exhibits an increase from -0.94 eV to -2.06 eV and -1.88 eV, respectively. Additionally, the length of the O-O bond was extended from 1.295 to 1.349 and 1.348 Å. This demonstrates that the presence of Ca and Sr promotes the binding of O_2 molecules. Simultaneously, the transfer of charge between the interfaces of O_2 and Ca/C-BN and Sr/C-BN is greatly increased, promoting the adsorption and subsequent activation of O_2 to produce $\cdot\text{O}_2$. The projected density of states (PDOS) for the chemisorption of O_2 on the three materials are shown in Fig. 4d. The upward and downward lines correspond to the α and β PDOS. The lack of complete overlap between the α and β PDOS suggests the presence of net magnetic moments in both gas-phase and chemisorbed substances [40]. Once O_2 is adsorbed onto the catalyst, the catalyst's electrons are transferred to the π^* orbit of O_2 . This transfer leads to a reduction in the overall spin (as shown in Table S3) [41]. Additionally, the difference between the α and β PDOS is smaller compared to gas-phase O_2 . The difference in the α and β PDOS gap between O_2 adsorbed on Ca/C-BN and Sr/C-BN near the Fermi level is smaller than that of O_2 adsorbed on C-BN. This feature demonstrates that the magnetic moment of O_2 adsorbed on the other two catalysts is diminished compared to that adsorbed on C-BN due to a higher charge transfer from the catalyst. Fig. 4e indicates that the adsorption of O_2 on Ca and Sr atoms primarily occurs through the interaction between the d orbital of Ca/Sr and the p orbital of the O_2

molecule. The process of adsorption and activation of the H_2O molecule is analogous to that of the O_2 molecule (Fig. S10-S11). Ca/C-BN and Sr/C-BN catalysts exhibit greater adsorption capacity for H_2O molecules compared to C-BN. Additionally, the bond length of H_2O molecules on the surface of these catalysts is also increased, favoring further dissociation to $\cdot\text{OH}$. Fig. S12 displays the PDOS calculation results for the H_2O adsorption configuration on C-BN, Ca/C-BN, and Sr/C-BN, covering an energy range from -25 eV to 5 eV. The Fig. illustrates how the energy of the molecular orbital of water decreases to different extents upon adsorption on the catalyst surface. These energy transfers can be attributed to the interaction with the substrate. The primary mechanism responsible for the adsorption of H_2O onto Ca and Sr atoms is the interaction between the p/d hybrid orbitals of Ca/Sr and the p orbital of oxygen in the H_2O molecule.

To investigate the active oxygen species generated during the photocatalytic reaction, we detected the electron spin resonance (ESR) signal by introducing suitable spin trapping reagents [42,43]. This allowed us to measure the signals of hydroxyl and superoxide radicals (Fig. 5a-b). The signal intensity of Ca/C-BN and Sr/C-BN is noticeably increased when exposed to Xenon lamp, in comparison to C-BN. We conducted a detailed analysis of the formation mechanism of $\cdot\text{O}_2$ and $\cdot\text{OH}$ on various catalyst surfaces using DFT calculations. Fig. 5c depicts that when determining the adsorption of O_2 and $\cdot\text{O}_2$, the initial magnetic moments

of oxygen atoms in O_2 are assigned as (1, 1) and (0, 1) respectively. The energy barrier for the formation of $\cdot\text{O}_2$ is -0.43, -1.57, and -1.50 eV for C-BN, Ca/C-BN, and Sr/C-BN, respectively. Ca/C-BN and Sr/C-BN exhibit a greater advantage in the formation of $\cdot\text{O}_2$. The energy barrier for H_2O dissociation is -2.85, -3.18, and -3.15 eV for C-BN, Ca/C-BN, and

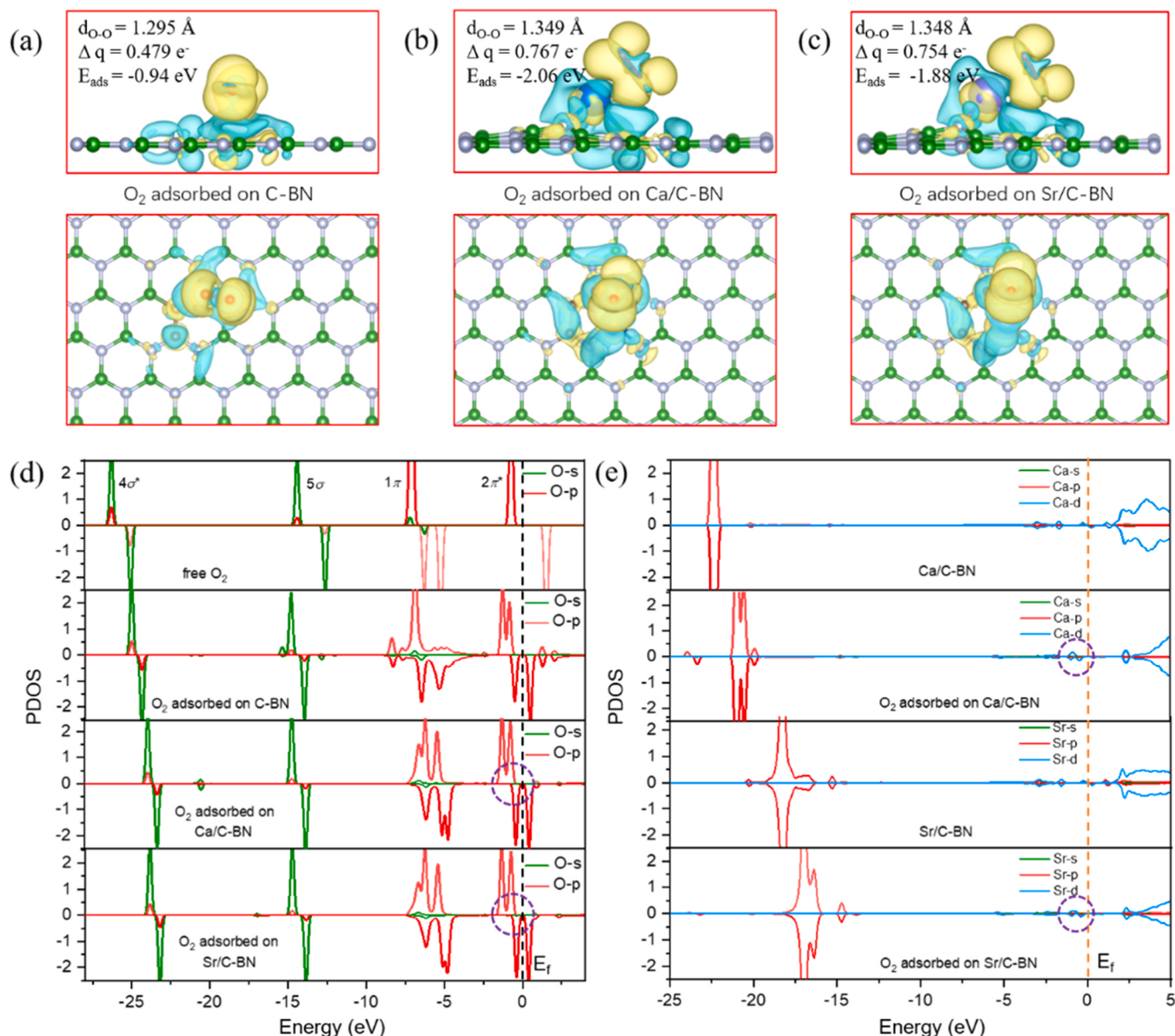


Fig. 4. The differential charge density (yellow area refers to charge accumulation and blue area refers to charge loss) distributions for O_2 on (a) C-BN, (b) Ca/C-BN and (c) Sr/C-BN. (d) PDOS of free and adsorbed O_2 on C-BN, Ca/C-BN and Sr/C-BN. (e) Ca, Sr atom PDOS of O_2 adsorbed on Ca/C-BN and Sr/C-BN.

Sr/C-BN, respectively. Similarly, Ca/C-BN and Sr/C-BN also demonstrate a greater advantage in facilitating the $\cdot OH$ formation. The oxidation of NO primarily occurs through two oxidative pathways dominated by $\cdot O_2$ or $\cdot OH$ [44]. The abundant ROS produced by the activation of O_2 and H_2O can facilitate the direct conversion of NO to NO_3 . Additionally, NO_2 adsorbed on the catalyst surface can be further converted to NO_3 , suppressing the formation of NO_2 (g). This process will be discussed in the section on photocatalytic mechanisms.

3.4. Photocatalytic performance and mechanism

To assess the effectiveness of the samples in eliminating the target pollutant NO under exposure to light, we conducted a test to evaluate the catalytic oxidation capacity of the three samples towards NO over a period of 1 h. The experiment was conducted in an environment with a NO concentration ranging from 500 to 600 ppb, and a xenon lamp was utilized to simulate sunlight. Fig. 6a demonstrates that the photocatalytic activity of C-BN is minimal. The conventional C-BN material exhibits a NO removal rate of less than 30% within 40 min, and the

efficiency of NO removal after 60 min of light exposure is merely 21.8%. The samples that were prepared with the introduction of Ca and Sr metals exhibited enhanced photocatalytic performance. Specifically, the removal efficiency of NO reached 57.8% and 54. 9% respectively after 60 min of exposure to light. Furthermore, we performed a recycling experiment on the photocatalytic oxidation of NO to investigate the durability of the catalyst (Fig. 6c). Following five cycles, the photocatalytic efficiency of all three catalysts exhibited a certain degree of decline. The decline in performance can be ascribed to the existence of oxidation products (NO_2 or NO_3) that are impeding specific active sites on the catalyst surface, and the photocatalytic performance of the catalyst can be efficiently restored by employing deionized water to cleanse and eliminate these products. Using ion chromatography, we conducted a detailed analysis of the NO_2 and NO_3 content in the washing solution (Table S4). Based on this result, we determined the selectivity of the oxidation products of NO. Fig. 6e demonstrates that the incorporation of Ca or Sr significantly improves the catalyst's ability to endure deep oxidation for NO, resulting in a NO_3 selectivity of 97.8% and 97.6% respectively. Fig. 6b, d shows that the introduction of alkali metals as

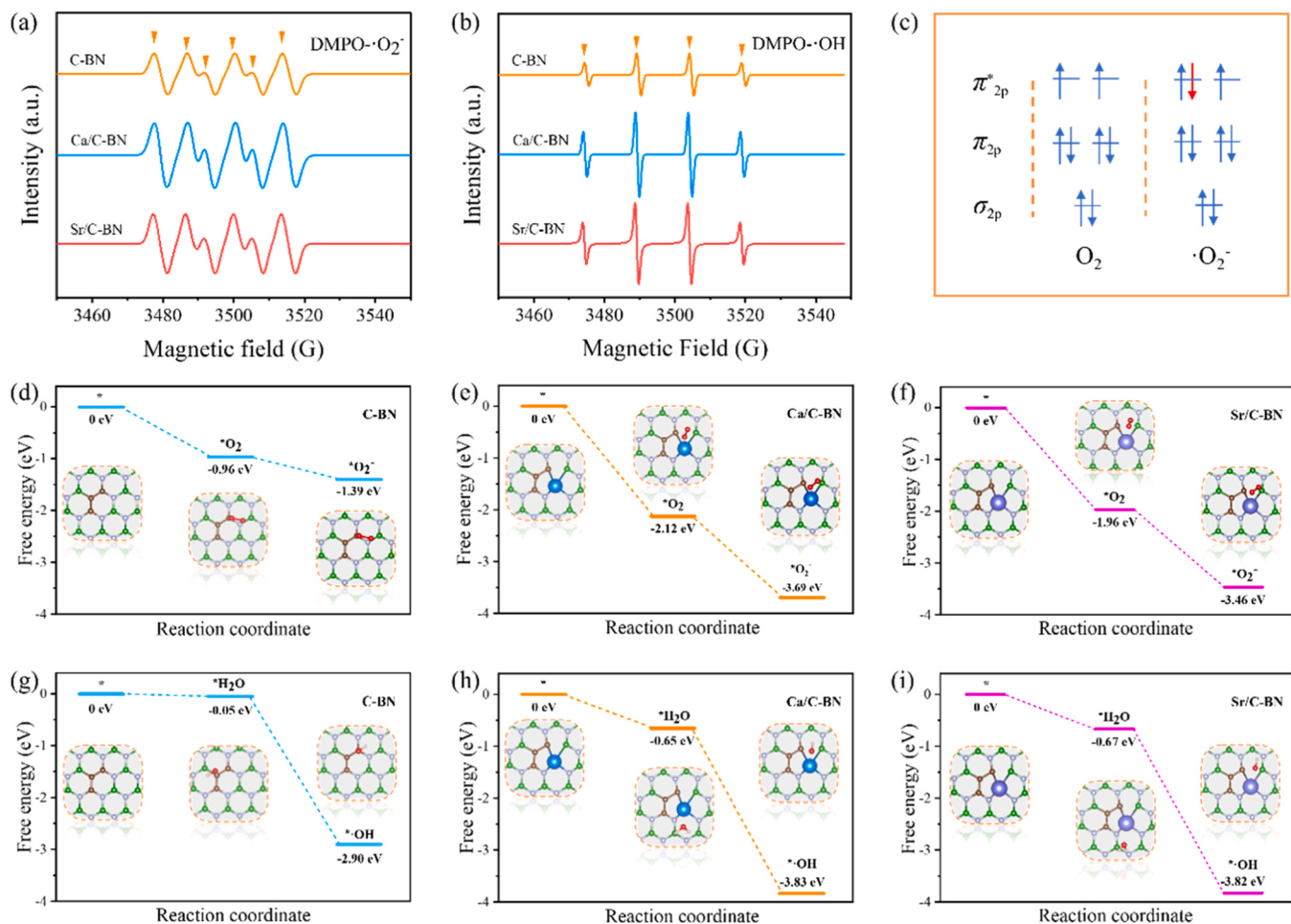


Fig. 5. ESR spectra of (a) DMPO- $\cdot\text{O}_2^-$ and (b) DMPO- $\cdot\text{OH}$ under the irradiation of a Xenon lamp. (c) The molecule orbital of O_2 and $\cdot\text{O}_2^-$. (d)-(f) Free energy change against the reaction coordinate for $\cdot\text{O}_2$ formation on different catalysts. (g)-(i) Free energy change against the reaction coordinate for $\cdot\text{OH}$ formation on different catalysts.

catalysts significantly reduces the emission of NO_2 (<10 ppb) from the two materials. The emission level is significantly lower than the primary and secondary national ambient air quality standards (NO_2 , EPA-456/F-99-006a, 53 ppb) established by the U.S. Environmental Protection Agency. To investigate the

oxidation mechanism of NO on the catalyst surface, we employed in-situ infrared technology for examining the adsorption and reaction products of NO on the surfaces of C-BN, Sr/C-BN, and Ca/C-BN samples. Fig. 6f-h demonstrates that the infrared peaks observed at 1330–1306 cm^{-1} and 925–920 cm^{-1} correspond to N_2O_4 . It is noteworthy that N_2O_4 , in conjunction with ROS, readily produces NO_3^- . Peaks ranging from 1675 to 1670 cm^{-1} can be identified as NO_2 and peaks ranging from 1558 to 1540 cm^{-1} can be determined as different vibration forms of NO_3^- . Furthermore, we conducted further studies on the catalytic surface's oxidation mechanism of NO using DFT calculation. Fig. 6i illustrates that the three catalysts have a greater tendency to generate $\cdot\text{HNO}_3$ in comparison to gaseous NO_2 . Simultaneously, the Ca/C-BN surface exhibits the highest energy barrier for the conversion of NO_2 from an adsorbed state to a gaseous state. This suggests that the generated NO_2 readily adsorbs onto the surface, facilitating its subsequent conversion to NO_3^- . This observation is consistent with the significant selectivity of Ca/C-BN that was observed during the experimental process.

4. Conclusion

This study demonstrates the efficacy of alkaline earth metal coordination materials utilizing C-BN as a matrix for the effective elimination of NO and storage of NO_3^- . The findings demonstrate that the photocatalytic oxidation of NO by Ca/C-BN and Sr/C-BN is more effective than that of C-BN, achieving a NO_3^- selectivity of > 97%. From a functional perspective, the addition of alkaline earth metals such as Ca and Sr can impede the recombination of charge, while increasing the absorption of harmful intermediate NO_2 and facilitating the highly specific conversion of NO to NO_3^- . This study offers valuable insights for the future advancement of exceptionally efficient catalysts for the removal of NO.

CRediT authorship contribution statement

Yumei Zhang: Formal analysis. **Qingzhi Luo:** Resources, Investigation. **Jing An:** Methodology. **Huiying Mu:** Software. **Huaiyu Zhang:** Software. **Yandong Duan:** Writing – review & editing, Writing – original draft, Supervision, Resources, Methodology, Funding acquisition, Formal analysis, Conceptualization. **Desong Wang:** Supervision, Resources, Formal analysis, Conceptualization. **Wanyu Zhang:** Writing – original draft, Methodology, Investigation, Formal analysis, Data curation. **Huanhuan Bai:** Data curation. **Bibo Ma:** Formal analysis, Data curation. **Lin Wang:** Formal analysis.

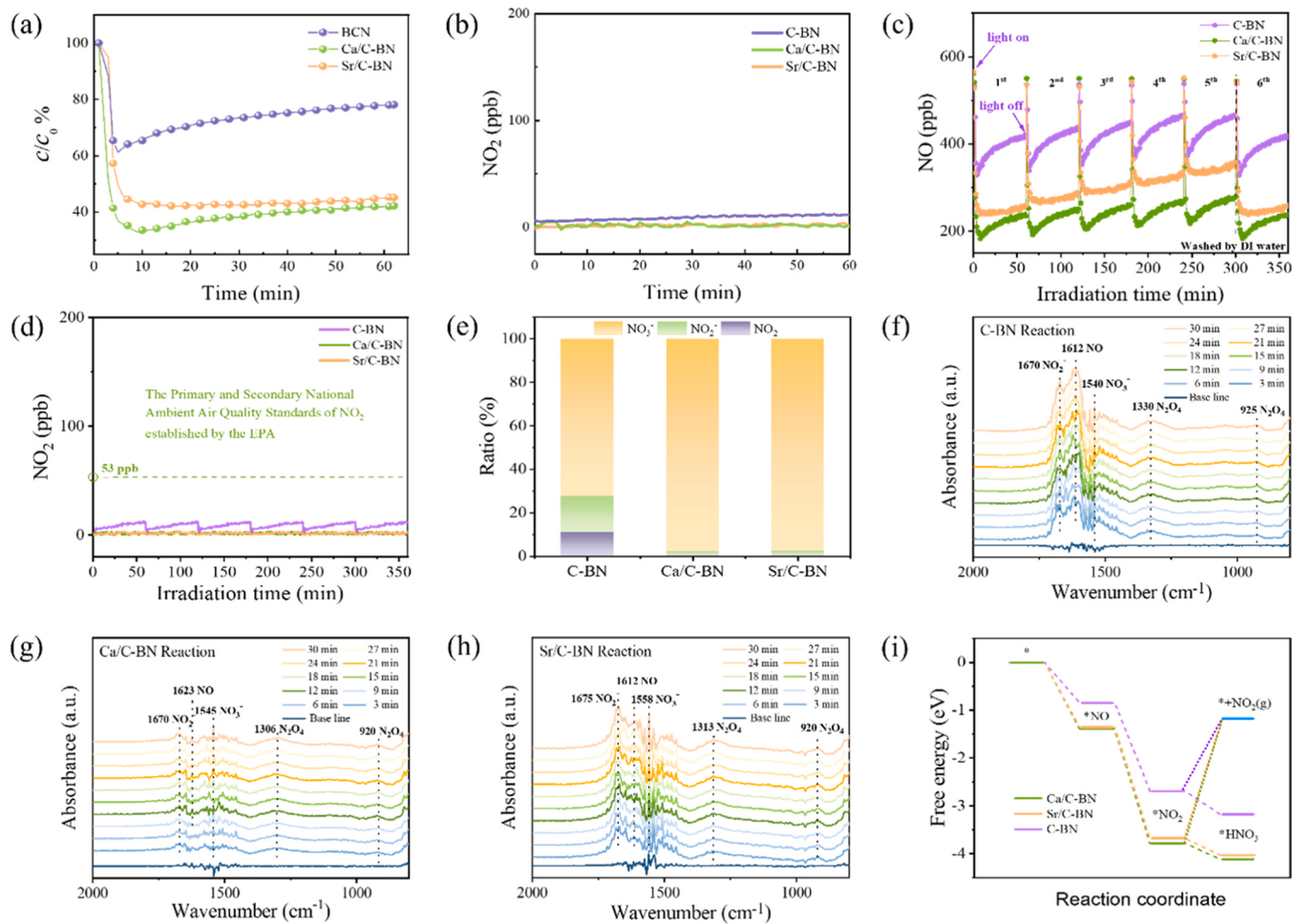


Fig. 6. (a) The variation of NO concentration on C-BN, Ca/C-BN and Sr/C-BN samples with reaction time. (b) The concentration of NO₂ on C-BN, Ca/C-BN, Sr/C-BN samples with reaction time. (c)-(d) Multicycle photocatalytic removal of NO on C-BN, Ca/C-BN and Sr/C-BN under light. (e) Distribution of NO oxidation products over C-BN, Ca/C-BN and Sr/C-BN. In-situ FTIR curves of NO oxidation on (f) C-BN, (g) Ca/C-BN, and (h) Sr/C-BN samples under light conditions. (i) Energy profile for the conversion of ^{*}NO to NO₂(g)/^{*}HNO₃ on the C-BN, Ca/C-BN and Sr/C-BN. The symbol "*" denotes the state of surface adsorption.

Declaration of Competing Interest

The authors declare that they have no known competing financial interests or personal relationships that could have appeared to influence the work reported in this paper.

Data Availability

No data was used for the research described in the article.

Acknowledgements

This work was supported by the Science and Technology Project of Hebei Education Department (ZD2022122), National Natural Science Foundation of China (No. 22278349) and Natural Science Foundation of Hebei Province (No. B2021208007). The theoretical work was carried out at Bianshui Riverside Supercomputing Center (BRSC). The authors extend their gratitude to Liya Sun from Shiyanjia Lab (www.shiyanjia.com) for providing invaluable assistance with the TEM analysis.

Appendix A. Supporting information

Supplementary data associated with this article can be found in the online version at [doi:10.1016/j.apcatb.2024.124241](https://doi.org/10.1016/j.apcatb.2024.124241).

References

- [1] P. Granger, V.I. Parvulescu, Catalytic NO_x abatement systems for mobile sources: from three-way to lean burn after-treatment technologies, *Chem. Rev.* 111 (2011) 3155–3207.
- [2] J.T. Kim, C.W. Lee, H.J. Jung, H.J. Choi, A. Salman, S.P. Sasikala, S.O. Kim, Application of 2D materials for adsorptive removal of air pollutants, *ACS Nano* 16 (2022) 17687–17707.
- [3] C.X. Hu, L.G. Wei, T. Wu, C.M. Yue, R.T. Guo, Minireview and perspective of one-dimensional manganese oxide nanostructures for the removal of air pollutants, *Energy Fuels* 37 (2023) 10886–10899.
- [4] H. Li, H. Zhu, Y. Shi, H. Shang, L. Zhang, J. Wang, Vacancy-rich and porous NiFe-layered double hydroxide ultrathin nanosheets for efficient photocatalytic NO oxidation and storage, *Environ. Sci. Technol.* 56 (2022) 1771–1779.
- [5] S. Li, H. Shang, Y. Tao, P. Li, H. Pan, Q. Wang, S. Zhang, H. Jia, H. Zhang, J. Cao, B. Zhang, R. Zhang, G. Li, Y. Zhang, D. Zhang, H. Li, Hydroxyl radical-mediated efficient photoelectrocatalytic NO oxidation with simultaneous nitrate storage using a flow photoanode reactor, *Angew. Chem. Int. Ed.* 135 (2023) e202305538.
- [6] V. Muñoz, C. Casado, S. Suárez, B. Sánchez, J. Marugán, Photocatalytic NO_x removal: Rigorous kinetic modelling and ISO standard reactor simulation, *Catal. Today* 326 (2019) 82–93.
- [7] V.H. Nguyen, B.S. Nguyen, C.W. Huang, T.T. Le, C.C. Nguyen, T.T.N. Le, D. Heo, Q. V. Ly, Q.T. Trinh, M. Shokouhimehr, C. Xia, S.S. Lam, D.V.N. Vo, S.Y. Kim, Q.V. Le, Photocatalytic NO_x abatement: recent advances and emerging trends in the development of photocatalysts, *J. Clean. Prod.* 270 (2020) 121912.
- [8] B. Rhimi, M. Padervand, H. Jouini, S. Ghasemi, D.W. Bahneemann, C. Wang, Recent progress in NO_x photocatalytic removal: surface/interface engineering and mechanistic understanding, *J. Environ. Chem. Eng.* 10 (2022) 108566.
- [9] D. Saini, A.K. Garg, C. Dalal, S.R. Anand, S.K. Sonkar, A.K. Sonker, G. Westman, Visible light promoted photocatalytic applications of carbon dots: a review, *ACS Appl. Nano Mater.* 5 (2022) 3087–3109.
- [10] J. Zhao, C. Li, X.Y. Du, Y.C. Zhu, S.H. Li, X. Liu, C.X. Liang, Q. Yu, L. Huang, K. Yang, Recent progress of carbon dots for air pollutants detection and

photocatalytic removal: synthesis, modifications, and applications, *Small* 18 (2022) 2200744.

[11] S. Hu, M. Zhu, Ultrathin two-dimensional semiconductors for photocatalysis in energy and environment applications, *ChemCatChem* 11 (2019) 6147–6165.

[12] Y. Zang, L.K. Li, S.Q. Zang, Recent development on the alkaline earth MOFs (AEMOFs), *Coord. Chem. Rev.* 440 (2021) 213955.

[13] L.A. Freeman, J.E. Walley, R.J. Gilliard, Synthesis and reactivity of low-oxidation-state alkaline earth metal complexes, *Nat. Synth.* 1 (2022) 439–448.

[14] X. Wu, L. Zhao, J. Jin, S. Pan, W. Li, X. Jin, G. Wang, M.F. Zhou, G. Frenking, Observation of alkaline earth complexes $M(CO)_8$ ($M=Ca, Sr, or Ba$) that mimic transition metals, *Science* 361 (2018) 912–916.

[15] T.T. Liu, D.D. Zhai, B.T. Guan, Z.J. Shi, Nitrogen fixation and transformation with main group elements, *Chem. Soc. Rev.* 51 (2022) 3846–3861.

[16] M. Zhou, G. Frenking, Transition-metal chemistry of the heavier alkaline earth atoms Ca, Sr, and Ba, *Acc. Chem. Res.* 54 (2021) 3071–3082.

[17] Q. Wang, S. Pan, S. Lei, J. Jin, G. Deng, G. Wang, L.L. Zhao, M.F. Zhou, G. Frenking, Octa-coordinated alkaline earth metal-dinitrogen complexes $M(N_2)_8$ ($M=Ca, Sr, Ba$), *Nat. Commun.* 10 (2019) 3375.

[18] C. Färber, P. Stegner, U. Zenneck, C. Knüpfer, G. Bendt, S. Schulz, S. Harder, Teaming up main group metals with metallic iron to boost hydrogenation catalysis, *Nat. Commun.* 13 (2022) 3210.

[19] Z.W. Qu, H. Zhu, R. Streubel, S. Grimme, Organo-group 2 metal-mediated nucleophilic alkylation of benzene: Crucial role of strong cation- π interaction, *ACS Catal.* 13 (2023) 1686–1692.

[20] H.W.T. Morgan, A.N. Alexandrova, Electron counting and high-pressure phase transformations in metal hexaborides, *Inorg. Chem.* 61 (2022) 18701–18709.

[21] W. Cui, J. Li, Y. Sun, H. Wang, G. Jiang, S.C. Lee, F. Dong, Enhancing ROS generation and suppressing toxic intermediate production in photocatalytic NO oxidation on O/Ba co-functionalized amorphous carbon nitride, *Appl. Catal., B* 237 (2018) 938–946.

[22] M. Zhou, G. Dong, J. Ma, F. Dong, C. Wang, J. Sun, Photocatalytic removal of NO by intercalated carbon nitride: The effect of group IIA element ions, *Appl. Catal., B* 273 (2020) 119007.

[23] M. Zhou, G. Dong, F. Yu, Y. Huang, The deep oxidation of NO was realized by Sr multi-site doped g-C₃N₄ via photocatalytic method, *Appl. Catal. B* 256 (2019) 117825.

[24] N. Shi, L. Li, P. Gao, X. Jiang, J. Hao, C. Ban, R.G. Zhang, Z.X. Liu, Synthesis of two-dimensional hexagonal boron nitride and mid-infrared nanophotonics, *ACS Appl. Electron. Mater.* 5 (2023) 34–65.

[25] M. Rafiq, X.Z. Hu, Z.L. Ye, A. Qayum, H. Xia, L.S. Hu, F.S. Lu, P.K. Chu, Recent advances in structural engineering of 2D hexagonal boron nitride electrocatalysts, *Nano Energy* 91 (2022) 106661.

[26] W. Jiang, C. Liu, X. Ma, X. Yu, S.B. Hu, X. Li, L.A. Burton, Y. Liu, Y.Y. Chen, P. Guo, X.Y. Kong, L. Bellaiche, W. Ren, Anomalous ferroelectricity and double-negative effects in bilayer hexagonal boron nitride, *Phys. Rev. B* 106 (2022) 054104.

[27] M.N. Ivanova, Y.A. Vorotnikov, E.E. Plotnikova, M.V. Marchuk, I.P. Asanov, A.R. Tsygankova, E.D. Grayfer, V.E. Fedorov, M.A. Shestopalov, Hexamolybdenum clusters supported on exfoliated h-BN nanosheets for photocatalytic water purification, *Inorg. Chem.* 59 (2020) 6439–6448.

[28] F. Guo, P. Yang, Z. Pan, X.N. Cao, Z. Xie, X.C. Wang, Carbon-doped BN nanosheets for the oxidative dehydrogenation of ethylbenzene, *Angew. Chem. Int. Ed.* 129 (2017) 8343–8347.

[29] J. Guo, Y. Duan, T. Wu, W. Zhang, L. Wang, Y. Zhang, Q. Luo, Q. Lu, Y. Zhang, H. Mu, H. Zhang, Q. Han, D. Wang, Atomically dispersed cerium sites in carbon-doped boron nitride for photodriven CO₂ reduction: Local polarization and mechanism insight, *Appl. Catal., B* 324 (2023) 122235.

[30] A. Kan, Y. Duan, J. Guo, T. Wu, L. Wang, Y. Zhang, Q. Luo, Q. Lu, Y. Zhang, Y. Liang, G. Yang, H. Zhang, H. Mu, Q. Han, D. Wang, Cobalt single atom induced catalytic active site shift in carbon-doped bn for efficient photodriven CO₂ reduction, *Appl. Surf. Sci.* 616 (2023) 156451.

[31] C. Huang, C. Chen, M.W. Zhang, L.H. Lin, X. Ye, S. Lin, M. Antonietti, X.C. Wang, Carbon-doped BN nanosheets for metal-free photoredox catalysis, *Nat. Commun.* 6 (2015) 7698.

[32] Q. Wan, F. Wei, Z. Ma, M. Anpo, S. Lin, Novel Porous boron nitride nanosheet with carbon doping: potential metal-free photocatalyst for visible-light-driven overall water splitting, *Adv. Theor. Simul.* 2 (2019) 1800174.

[33] G. Kresse, J. Furthmüller, Efficient iterative schemes for ab initio total-energy calculations using a plane-wave basis set, *Phys. Rev. B* 54 (1996) 11169.

[34] G. Kresse, J. Furthmüller, Efficiency of ab initio total energy calculations for metals and semiconductors using a plane-wave basis set, *Comput. Mater. Sci.* 6 (1996) 15–50.

[35] J.P. Perdew, K. Burke, M. Ernzerhof, Generalized gradient approximation made simple, *Phys. Rev. Lett.* 77 (1996) 3865.

[36] S. Grimme, J. Antony, S. Ehrlich, H. Krieg, A consistent and accurate ab initio parametrization of density functional dispersion correction (DFT-D) for the 94 elements H–Pu, *J. Chem. Phys.* 132 (2010) 154104.

[37] S. Grimme, S. Ehrlich, L. Goerigk, Effect of the damping function in dispersion corrected density functional theory, *J. Comput. Chem.* 32 (2011) 1456–1465.

[38] M. Liu, Y. Pang, B. Zhang, P. Luna, O. Voznyj, J. Xu, X. Zheng, C.T. Dinh, F. Fan, C. Cao, F.P.G. Arquer, T.S. Safaei, A. Mepham, A. Klinkove, E. Kumacheva, T. Fileteer, D. Sinton, S.O. Kelly, E.H. Sargent, Enhanced electrocatalytic CO₂ reduction via field-induced reagent concentration, *Nature* 537 (2016) 382–386.

[39] J. Li, S. Chen, F. Quan, G. Zhan, F. Jia, Z. Ai, L. Zhang, Accelerated dinitrogen electroreduction to ammonia via interfacial polarization triggered by single-atom protrusions, *Chem* 6 (2020) 885–901.

[40] M.M. Montemore, M.A. van Spronsen, R.J. Madix, C.M. Friend, O₂ Activation by metal surfaces: Implications for bonding and reactivity on heterogeneous catalysts, *Chem. Rev.* 118 (2017) 2816–2862.

[41] R. Pai, L.M. Wang, Y. Pei, L.S. Wang, X. Zeng, Unraveling the mechanisms of O₂ activation by size-selected gold clusters: transition from superoxo to peroxy chemisorption, *J. Am. Chem. Soc.* 134 (2012) 9438–9445.

[42] H. Li, H. Ji, J. Liu, W. Liu, F. Li, Z. Shen, Interfacial modulation of ZnIn₂S₄ with high active Zr-S₄ sites for boosting photocatalytic activation of oxygen and degradation of emerging contaminant, *Appl. Catal. B* 328 (2023) 122481.

[43] F. Guo, H. Zhang, H. Li, Z. Shen, Modulating the oxidative active species by regulating the valence of palladium cocatalyst in photocatalytic degradation of ciprofloxacin, *Appl. Catal. B* 306 (2022) 121092.

[44] H. Shang, H. Jia, P. Li, H. Li, W. Zhang, S. Li, Q. Wang, S. Xiao, D. Wang, G. Li, D. Zhang, Highly selective and efficient photocatalytic NO removal: Charge carrier kinetics and interface molecular process, *Nano Res.* 17 (2024) 1003–1026.